The cross-sectional shape of tidal sandbanks: Modeling and observations

Pieter C. Roos, Suzanne J. M. H. Hulscher, and Michiel A. F. Knaapen
Water Engineering and Management, Faculty of Engineering Technology, University of Twente, Enschede, Netherlands

Ruud M. J. Van Damme
Department of Applied Mathematics, Faculty of Electrical Engineering, Mathematics and Computer Science, University of Twente, Enschede, Netherlands

Received 29 July 2003; revised 11 February 2004; accepted 20 February 2004; published 16 April 2004.

[1] To improve our understanding of tidal sandbank dynamics, we have developed a nonlinear morphodynamic model. A crucial property of the model is that it fully resolves the dynamics on the fast (tidal) timescale, allowing for asymmetric tidal flow with an M_0, M_2, and M_4 component. This approach, extending earlier research on the formation of tidal sandbanks, leads to equilibrium profiles. Their heights (60–90% of the water depth) and shapes are controlled by the mode of sediment transport and the hydrodynamic conditions. Bed load transport under symmetrical tidal conditions leads to high spiky banks. Several mechanisms tend to lower and smooth these profiles, such as the relaxation of suspended sediment, wind wave stirring, and tidal asymmetry. This last causes the profiles to be asymmetric, as well. The morphodynamic equilibrium expresses a tidally averaged balance between a destabilizing flux due to fluid drag and the downslope transport induced by both tidal flow and wind wave stirring. The modeled profiles are in fair agreement with observations from the North Sea. *INDEX TERMS:* 3210 Mathematical Geophysics: Modeling; 3220 Mathematical Geophysics: Nonlinear dynamics; 3022 Marine Geology and Geophysics: Marine sediments—processes and transport; 4219 Oceanography: General: Continental shelf processes; 4560 Oceanography: Physical: Surface waves and tides (1255); *KEYWORDS:* morphodynamics, tidal sandbanks, equilibrium profiles

Citation: Roos, P. C., S. J. M. H. Hulscher, M. A. F. Knaapen, and R. M. J. Van Damme (2004), The cross-sectional shape of tidal sandbanks: Modeling and observations, *J. Geophys. Res.*, *109*, F02003, doi:10.1029/2003JF000070.

1. Introduction

[2] Improving our understanding of offshore seabed morphology is a challenge of both academic and practical interest. Tidal currents, waves, and sediment motion interact in a complex way, which is manifested by the variety of rhythmic bed forms covering the seabed. Despite considerable advances, these large-scale seabed dynamics are still not fully understood. Practical issues include predicting the long-term morphodynamic impact of a large-scale sandpit.

[3] Tidal sandbanks, the largest offshore bed features, occur in rhythmic patches throughout the North Sea (Figure 1). They are tens of kilometers long, 5–10 km wide, and tens of meters high [*Dyer and Huntley*, 1999]. Bank crests (on the Northern Hemisphere) usually have a counterclockwise orientation to the peak tidal flow, ranging from 0° to 20° [*Kenyon et al.*, 1981]. Finally, most bank shapes display a cross-sectional left-right asymmetry, which emphasizes the role of asymmetries in the forcing of the system.

[4] Past research into sandbank dynamics mainly focused on the process of formation. *Huthnance* [1982a] was the first to show that they may arise as an inherent instability of a flat seabed subject to tidal flow and bed load sediment transport. His approach is process-based, i.e., based on mathematical formulations of the physical processes involved. The underlying hydrodynamic mechanism, known as tidal rectification, describes the adjustment of tidal flow obliquely approaching a sandbank [*Zimmerman*, 1981; *Robinson*, 1983; *Pattiaratchi and Collins*, 1987; *Roos and Hulscher*, 2003]. The cross-bank component is accelerated by continuity; the along-bank component is decelerated by bottom friction, acting more strongly in shallower water. This flow deflection affects the tidally averaged sediment transport pattern, causing upslope sediment transport and hence bank growth. Furthermore, the along-bank flow component is either accelerated or decelerated by Coriolis effects, depending on the crest orientation. For counterclockwise orientations (Northern Hemisphere), this amplifies the frictionally induced flow deflection and hence bank growth such that it is strongest for a particular counterclockwise crest angle. The model also predicts a preferred wavelength. Both orientation and wavelength are in fair agreement with banks observed in

0148-0227/04/2003JF000070$09.00

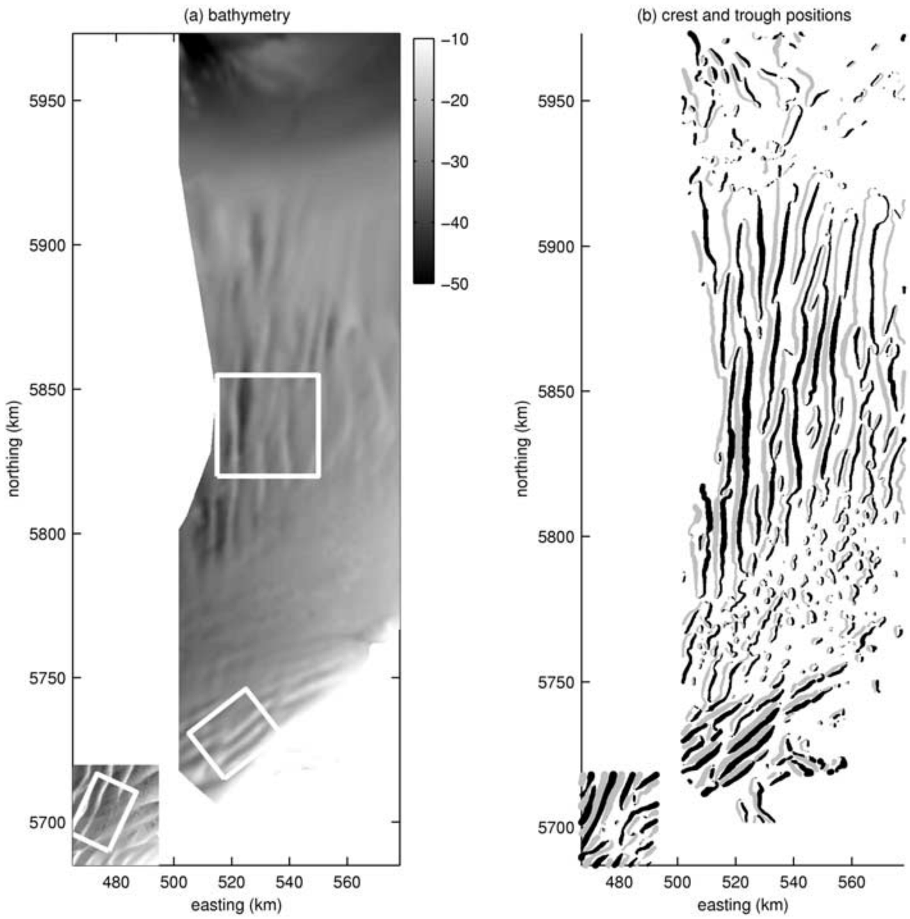

Figure 1. Seabed topography in the Southern Bight of the North Sea. (a) Bathymetry, showing three boxed areas to be analyzed further in section 5. Regions without data are indicated in white, such as the U.K. continental shelf (left) and the Dutch and Belgian mainland (bottom right). (b) Crest and trough positions of large-scale features (in red and blue, respectively), with line thickness proportional to bank height. See the acknowledgments for data sources. See color version of this figure at back of this issue.

the North Sea. These results were later extended to include suspended load sediment transport, wind waves, tidal ellipticity, and tidal asymmetry in the forcing [*De Vriend*, 1990; *Hulscher et al.*, 1993; *Roos et al.*, 2001]. The main limitation of these theories is their linearity in the bed amplitude, which limits their validity to banks that are low compared to the water depth. If banks have attained a finite amplitude, a nonlinear approach is required.

[5] How to model the finite amplitude evolution toward equilibrium profiles is still an unresolved issue. Extending his linear analysis, *Huthnance* [1982a] indeed found equilibrium bank profiles, and he identified wind wave erosion as a crucial mechanism. However, his treatment of the hydrodynamics was rather simplified (using a block flow, omitting inertial terms, and neglecting the Coriolis force). This criticism also applies to *Idier and Astruc* [2003], who estimated the equilibrium bank height at about 90% of the maximum water depth using a nonlinear numerical method. Their estimate was based on a morphostatic approach, i.e., on the initial bed response obtained for a series of simulations with sinusoidal banks of different amplitudes. We note that *Idier and Astruc* [2003] validated their nonlinear numerical method by reproducing the analytically obtained growth characteristics from linear theory. *Komarova and Newell* [2000] studied an alternative mechanism of bank formation related to the nonlinear interaction of tidal sandwaves, a smaller-scale bed feature. Their two-dimensional vertical approach neglected the horizontal dimension perpendicular to the flow, so the bank orientation could not be resolved. Therefore it is unclear whether their results are supported by field observations.

[6] The aim of this paper is to model equilibrium sandbank profiles in an alternative way. Our emphasis is on three topics not addressed by previous work: (1) the morphodynamic evolution to equilibrium shapes; (2) the influence of different tidal components on bank profiles; and (3) a qualitative comparison with bank shapes observed in the North Sea. We propose an idealized, process-based morphodynamic model, which allows for a harmonic tidal flow with an M_0, M_2, and M_4 component, considers both bed load and suspended load transport, and includes a depth-dependent wave-stirring mechanism. To establish

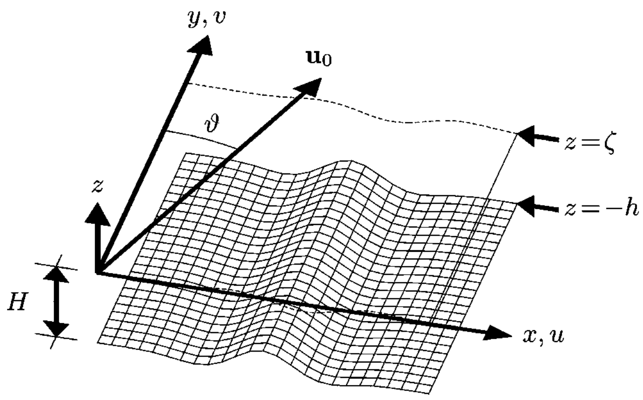

Figure 2. Definition sketch of the model geometry, also showing the basic (undisturbed) flow angle ϑ (section 2.3).

how the modeled profiles compare with observations, we have two data sets on the bathymetry of the Southern Bight of the North Sea at our disposal (Figure 1) (see the acknowledgments for data sources).

[7] This paper is organized as follows. In section 2 we describe the morphodynamic model, whereas section 3 explains the solution procedure, which follows a standard Galerkin approach. The results are presented in section 4 and compared qualitatively with North Sea data in section 5. Finally, sections 6 and 7 contain the discussion and conclusions, respectively.

2. Morphodynamic Model

2.1. Physical Mechanisms and Geometry

[8] We keep the model as simple as possible while retaining the essential physics. Following previous analysis [*Huthnance*, 1982a, 1982b; *De Vriend*, 1990; *Hulscher et al.*, 1993], we apply a depth-averaged approach to the flow, thus neglecting its vertical structure. To capture the mechanism of tidal rectification, we include the Coriolis force and a bed friction mechanism. The seabed is assumed to consist of noncohesive sediment of uniform size (typical grain size 100–600 μm). Besides a commonly adopted bed load transport formula, we choose to incorporate a mechanism for suspended load transport, as well. Observations from the Norfolk Banks [*Huntley et al.*, 1993] and the Middelkerke Bank [*Vincent et al.*, 1998] have shown that suspended load is indeed a significant mode of transport over tidal sandbanks, especially at the crests. Assuming fair weather and offshore conditions, we consider tidally dominated flows in which the role of wind waves is restricted to the stirring of sediment. We include this effect parametrically using a depth-dependent stirring term, which augments the local transport capacity.

[9] We restrict our work to topographies that vary in one horizontal dimension only. This assumption is supported by the predominantly one-dimensional character of real sandbanks (Figure 1). It also simplifies the analysis and requires the orientation between tidal forcing and the direction of spatial variations to be imposed a priori. Motivated by the rhythmic structure of observed banks, we apply a spatially periodic approach with a fixed domain length and periodic boundary conditions. For both quantities which need to be imposed externally, namely domain length and flow orientation, we take their preferred values from linear theory (section 3.1).

2.2. Model Equations

[10] Consider an offshore part of the sea, far away from coastal boundaries, with a mean depth H and where the water motion is driven by tidal flow with a dominating semidiurnal lunar component (period T = 12 hours, 25 min) and a maximum flow velocity U (typically $\sim$1 m s^{-1}). We define a three-dimensional coordinate system with horizontal coordinates $\mathbf{x} = (x, y)$, with x chosen as the direction of the spatial variations (Figure 2). Parameter values are listed in Table 1.

[11] The z axis points upward, with the free surface at $z = \zeta$ and the seabed at $z = -h$. Let $\mathbf{u} = (u, v)$ represent the depth-averaged flow field with components in the x and y direction, respectively. Within our one-dimensional approach the shallow water equations take the following form:

$$g\frac{\partial \zeta}{\partial x} + \frac{\partial u}{\partial t} + u\frac{\partial u}{\partial x} - fv + \frac{ru}{h} = P_x, \tag{1}$$

$$\frac{\partial v}{\partial t} + u\frac{\partial v}{\partial x} + fu + \frac{rv}{h} = P_y, \tag{2}$$

$$\frac{\partial (hu)}{\partial x} = 0. \tag{3}$$

Here g is the gravitational acceleration, $f = 2\Omega \sin\theta$ is a Coriolis parameter (where $\Omega = 7.292 \times 10^{-5}$ s^{-1} is the angular frequency of the Earth's rotation and θ is the latitude), and r is a linear friction coefficient. This friction coefficient is related to the drag coefficient c_D of the sediment according to $r = 8\, c_D U/(3\pi)$ [*Zimmerman*, 1982]. Furthermore, we have adopted the rigid-lid approach, in which the contribution of the free surface elevation to the local water depth is neglected. This is motivated by the small value of the (squared) Froude number $Fr^2 = U^2/(gH)$. In section 6.1 we will verify whether this assumption continues to be justified in the finite amplitude regime. Finally, the system is driven by a time-dependent pressure gradient (P_x, P_y). Owing to the propagating nature of the

Table 1. Parameters and Values, Typical for the Southern Bight of the North Sea

Description	Symbol	Value	Dimensions
Mean water depth	H	30	m
Maximum flow velocity	U	1	m s^{-1}
Angular frequency (M_2 tide)	σ	1.41×10^{-4}	rad s^{-1}
Gravitational acceleration	g	9.81	m s^{-2}
Coriolis parameter (52°N)	f	1.16×10^{-4}	s^{-1}
Linear friction coefficient	r	2.5×10^{-3}	m s^{-1}
Grain size	d	3×10^{-4}	m
Bed load transport coefficient	α_b	4×10^{-5}	m^{-1} s^2
Bed slope coefficient	λ	2	
Wave stirring parameter	U_w	0.25	m s^{-1}
Suspended load entrainment coefficient	α_s	4×10^{-5}	m^{-1} s^2
Suspended load deposition coefficient	γ	0.016	s^{-1}
Bed porosity	p	0.4	
(Squared) Froude number	Fr^2	0.0034	

tidal wave (wavelength ~700 km), this forcing should also be gradually varying in space, but in a local model we may represent it as spatially uniform. In section 2.3 the forcing is further specified in terms of the flow it generates in the case of a flat bed.

[12] As the divergences of the bed load flux control the bed evolution, only its component in the direction of spatial variations is morphodynamically relevant. Let q denote the x component of the volumetric bed load sediment flux, which we express in terms of the depth-averaged flow and the local bed slope according to

$$q = \alpha_b \left(|\mathbf{u}|^2 + \frac{1}{2} u_w^2 \right) \left(u + \lambda \frac{\partial h}{\partial x} \right). \tag{4}$$

This is a third power velocity law with proportionality coefficient α_b [*Van Rijn*, 1993], including a bed slope correction and a stirring term. The bed slope correction describes the downhill preference of moving sediment with coefficient $\lambda = \tilde{\lambda} U$, in which $\tilde{\lambda}$ is inversely proportional to the tangent of the angle of repose [see, e.g., *Sekine and Parker*, 1992]. The term $(1/2)u_w^2$ represents the stirring due to wind waves, in which u_w is a measure for the wave-induced near-bed orbital velocity amplitude. Stirring augments the amount of sediment transported by the tidal flow and should be stronger in shallow water. We therefore model it inversely proportional to the local water depth, according to

$$u_w = U_w \left(\frac{h}{H} \right)^{-m}, \tag{5}$$

with coefficient U_w (~0.25 m s^{-1}) and power m = 1. This integer value of m facilitates the analysis and approximates the values adopted in other studies (for example, *Calvete et al.* [2002] employed m = 0.8). We neglect the threshold for sediment motion.

[13] To model suspended load transport, we use an advection equation [*Schuttelaars and De Swart*, 1996]:

$$\frac{\partial c}{\partial t} + \frac{\partial (cu)}{\partial x} = \gamma (c_e - c). \tag{6}$$

Here c denotes the depth-integrated sediment concentration, i.e., the volume of suspended matter in the water column. The left-hand side of equation (6) describes spatial and temporal relaxation of suspended load, while the right-hand side models the exchange between bed and fluid column due to entrainment and deposition. The entrainment concentration c_e is assumed to depend nonlinearly on the flow velocity, with coefficient α_s:

$$c_e = \alpha_s \left(|\mathbf{u}|^2 + \frac{1}{2} u_w^2 \right). \tag{7}$$

We have again included a stirring term, as introduced in equation (5). By taking a quadratic dependence on the flow velocity rather than, for example, a cubic one [*Van Rijn*, 1993], we facilitate the analysis without qualitatively affecting the results. In equation (6), deposition is taken proportional to the local concentration, with coefficient γ. Following *Schuttelaars and De Swart* [1996], we use γ = w_s^2/κ_v, where w_s is settling velocity and κ_v = 0.1 m^2 s^{-1} is a diffusion coefficient that describes the mixing of sediment in the vertical. We neglect the horizontal diffusion of suspended matter.

[14] Finally, the bed evolves as a result of divergences of bed load flux and the difference between entrainment and deposition of suspended matter. As this process is much slower (decades to centuries) than the tidal timescale (12 hours, 25 min), only the tidally averaged effect effectively contributes to the bed evolution. To emphasize this separation of hydrodynamic and morphodynamic timescales, we describe the bed evolution as a function of a slow time $\tau = \tilde{\alpha} t$, expressed in units of years (hence $\tilde{\alpha}$ = 3.17 × 10^{-8}). This leads to

$$(1-p)\frac{\partial h}{\partial \tau} = \frac{\mu_b}{\tilde{\alpha}} \frac{\partial \langle q \rangle}{\partial x} + \frac{\mu_s \gamma}{\tilde{\alpha}} \left[\langle c_e - c \rangle + \lambda \frac{\partial}{\partial x} \left(\langle c_e \rangle \frac{\partial h}{\partial x} \right) \right]. \tag{8}$$

Here p is the bed porosity (typically $p \sim 0.4$) and $\langle \cdot \rangle \equiv T^{-1} \int_0^T dt$ means averaging over a tidal period T. The coefficients μ_s and μ_b have been introduced to control the relative importance of bed load and suspended load transport. In particular, this allows us to study the transport mechanisms isolated from each other. For suspended load transport we have further incorporated a diffusive bed slope mechanism, with coefficient λ. *Parker* [1978] and *Talmon et al.* [1995] have shown that suspended load is also susceptible to bed slope effects. We choose to include bed slope effects in such a way that they resemble the slope effects in the bed load case, i.e., also including a stirring component.

[15] Finally, we emphasize that our approach is based on standard scaling technique, which we do not present here for the sake of brevity. Details can be found, for example, in the work of *Hulscher et al.* [1993] for the scaling of hydrodynamics and bed load transport and in the work of *Schuttelaars and De Swart* [1996] for the scaling of suspended load transport.

2.3. Basic State

[16] Let h and $\phi \equiv (\zeta, u, v, q, c)$ denote the state of the system. The spatially uniform state

$$h_0 = H \qquad \phi_0 = (0, u_0, v_0, q_0, c_0) \tag{9}$$

is a solution to equations (1)–(8). It describes a flat bed subject to a spatially uniform and fast time-dependent flow and is called the basic state. From equations (1) and (2) the basic flow is related to the tidal forcing (P_x, P_y), which we choose such that it generates a bidirectional oscillatory flow at an angle ϑ with the y direction (see Figure 2):

$$\mathbf{u}_0(t) = j(t)(\sin \vartheta, \cos \vartheta). \tag{10}$$

Positive values of ϑ correspond to a counterclockwise bank orientation with respect to the flow. Next, the tidal signal $j(t)$ is given by

$$j(t) = j_0 + j_2 \cos(\sigma t) + j_4 \cos(2\sigma t - \varphi_4). \tag{11}$$

In this equation we consider three tidal components: a residual flow j_0, a semidiurnal lunar component j_2 of angular frequency σ (see Table 1), and its first overtide j_4, with a phase lag φ_4. The sediment transport pattern of the basic state is also spatially uniform so that following equation (8), the seabed remains flat: $\partial h_0/\partial\tau = 0$.

3. Solution Procedure

3.1. Linear Theory

[17] Let us now revisit the linear analysis, highlighting only the properties that are relevant for the subsequent nonlinear theory. Here the basic state (h_0 and ϕ_0) serves as starting point, and we expand

$$h = h_0 + h_1 \qquad \phi = \phi_0 + \phi_1. \tag{12}$$

The equations for the perturbed state h_1 and $\varphi_1 \equiv (\zeta_1, u_1, v_1, q_1, c_1)$ follow from substituting equation (12) into equations (1)–(8). In the linear theory the topographic perturbations are assumed to be small compared to the water depth such that nonlinear terms in h_1 and ϕ_1 can be neglected.

[18] We consider a sinusoidal bed perturbation

$$h_1 = H_1(\tau)e^{ikx} + \text{c. c.}, \tag{13}$$

with $H_1 = H_1^{\text{init}}$ at $\tau = 0$ and with c. c. denoting complex conjunction. The wave number k and the orientation ϑ with respect to the flow (equation (10)) can be seen as the characteristics of the perturbation. Following the mechanism of tidal rectification (as explained in section 1), the perturbation triggers flow and sediment transport responses $\mathbf{u}_1$, q_1, and c_1, respectively. They have a spatial structure similar to equation (13) and a temporal structure accounting for the generation of overtides due to tide-topography interaction. We write

$$\phi_1 = \left(\sum_{n=-N}^{N} \Phi_1^n e^{int}\right) e^{ikx} + \text{c. c.}, \tag{14}$$

with Fourier components $\Phi_1 \equiv (Z_1^n, U_1^n, V_1^n, Q_1^n, C_1^n)$, truncated at some N. Finally, solving the bed evolution equation (8) gives $\partial H_1/\partial\tau = \omega H_1$, which leads to

$$h = h_0 + \left[H_1^{\text{init}} e^{\omega\tau} e^{ikx} + \text{c. c.}\right], \tag{15}$$

i.e., exponential growth or decay, with ω representing the growth rate. Mathematically speaking, the eigenfunctions of the system are of the form of equation (13), ω being the corresponding eigenvalue. The growth rate is a complex number $\omega = \omega_r + i\omega_i$. Its real part controls the growth, while the imaginary part is associated with migration of the feature, the corresponding celerity being given by $c_{\text{mig}} = -\omega_i/k$.

[19] The perturbation, for which the real part of ω is largest, is termed the "fastest growing mode" (Figure 3). Its characteristics (wave number k_{fgm}, orientation ϑ_{fgm}, and growth rate ω_{fgm}) depend on the problem parameters (Table 1). From the linear perspective, this is clearly the most interesting mode as it will emerge initially from a slightly perturbed flat bed. For typical North Sea values the fastest growing mode indeed approximates the characteristics of tidal sandbanks observed there, even though the linear theory overestimates the angle between flow direction and bank crests. Further properties of the fastest growing mode can be found in the work of *Huthnance* [1982a], *De Vriend* [1990], *Hulscher et al.* [1993], and *Roos et al.* [2001].

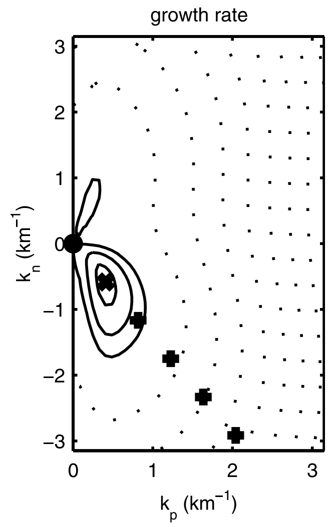

Figure 3. Modes to be used in the nonlinear analysis in the (k_p, k_n) plane with $k_p \equiv k\sin\vartheta$ and $k_n \equiv -k\cos\vartheta$. The fastest growing mode is denoted with a cross, the $k = 0$ mode with a circle, and the higher harmonics with pluses. Also plotted are the contours of the real part of growth rates from linear theory (solid contours are positive, dashed contours are negative, case A_s in Table 2).

[20] The lobes with positive growth rates always connect to the origin (Figure 3a). As a result, there is no control parameter for which near-critical conditions can be achieved while the fastest growing mode retains a finite, nonzero value.

3.2. Nonlinear Theory

[21] The nonlinear theory is not restricted to small perturbations of the basic flow. We follow a standard Galerkin approach, which has been used earlier in morphodynamic studies (see *Schuttelaars* [1998] for tidal embayments and *Calvete et al.* [2002] for shoreface-connected sand ridges). As pointed out in section 2, one-dimensionality and spatial periodicity force us to fix both the flow orientation ϑ and the Fourier box size $L \equiv 2\pi/k$. On the basis of linear theory, we take $(k, \vartheta) = (k_{\text{fgm}}, \vartheta_{\text{fgm}})$. Next, we write the topography as

$$h = \sum_{m=-M}^{M} H_m e^{ikmx}, \tag{16}$$

with Fourier components H_m. This expansion contains the $k = 0$ mode, the fastest growing mode from linear theory, as well as a finite number of higher harmonics (see the markers in Figure 3). We then expand the other state variables according to

$$\phi = \sum_{m=-M}^{M} \left(\sum_{n=-N}^{N} \Phi_m^n e^{i\sigma nt}\right) e^{ikmx}, \tag{17}$$

with Fourier components $\Phi_m^n \equiv (Z_m^n, U_m^n, V_m^n, Q_m^n, C_m^n)$, truncated in space and time at some M and N, respectively.

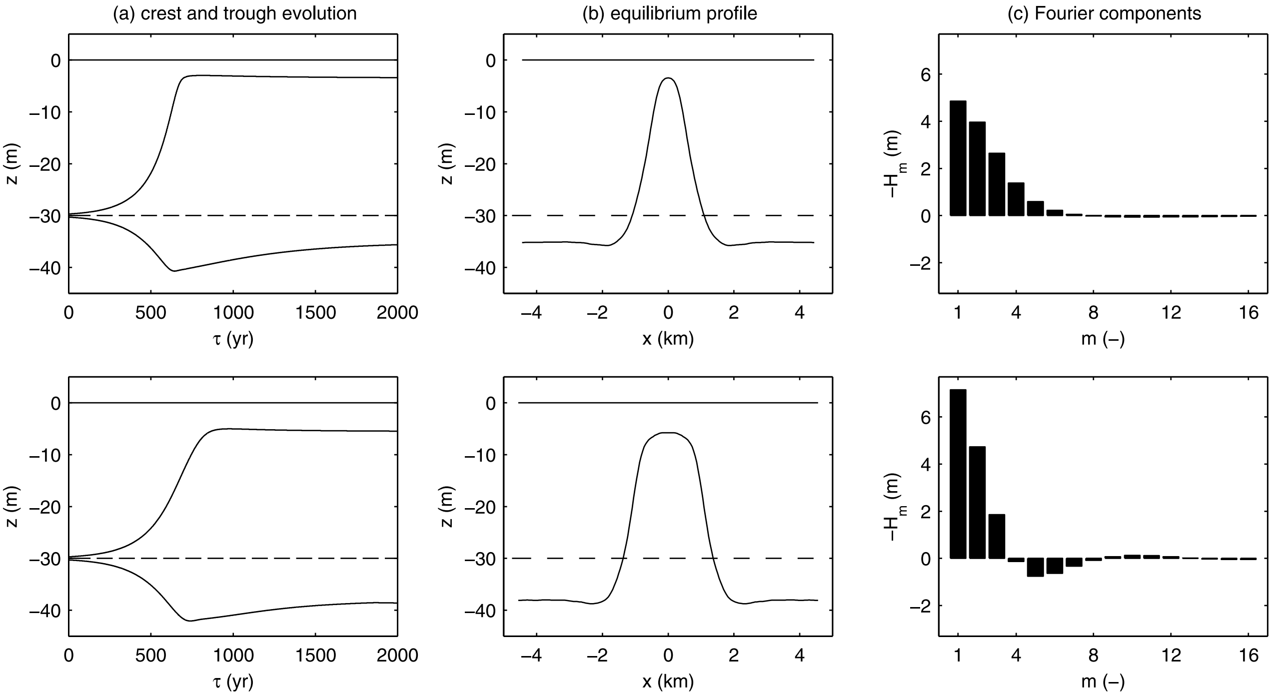

Figure 4. Finite amplitude evolution starting from a small perturbation with $H_1/H = 0.01$, for both (top) bed load transport (case A_b in Table 2) and (bottom) suspended load transport (case A_s in Table 2). (a) Evolution of crest $z = -h_{cr}$ and trough $z = -h_{tr}$ (as defined in Figure 5). (b) Cross-sectional shape of the equilibrium profile. (c) Real part of the corresponding Fourier spectrum H_m, not showing the average water depth H_0 = 30 m. Truncation numbers are M = 16 and N = 3.

Unlike linear theory, the nonlinear analysis allows us to consider any topography $h > 0$ which averages $\{h\}_0 = h_0$ over the domain. (Here $\{\cdot\}_0 \equiv L^{-1}\int_0^L \cdot\, dx$ represents spatial averaging over the domain.)

[22] From the continuity equation (3) the cross-bank flow is given by

$$u = \frac{\xi(t)}{h(x)}, \tag{18}$$

in which the integration constant $\xi(t)$ takes the role of the cross-bank water flux. It depends on the fast time, and we expand it as a harmonic time series $\xi(t) = \Sigma_n X^n e^i \sigma^{nt}$.

[23] The hydrodynamic unknowns X^n and V_m^n follow from substituting equation (18) into the momentum equations (1) and (2), then taking the spatial average $\{\cdot\}_0$ of the former and multiplying the latter with the local depth h. In Fourier space, this leads to

$$i\sigma n\left\{\frac{1}{h}\right\}_0 X^n - fV_0^n + r\left\{\frac{1}{h^2}\right\}_0 X^n = P_x^n \tag{19}$$

$$i\sigma n\{hv\}_m^n + ikm\{\xi v\}_m^n + f\{\xi\}_m^n + rV_m^n = P_y^n H_m. \tag{20}$$

Here $\{\cdot\}_m^n$ denotes the mth spatial and nth temporal Fourier component, which involves a convolution sum if the bracketed quantity is a product. Moreover, P_x^n and P_y^n are the Fourier components of the forcing (P_x, P_y). For $f = 0$, these equations decouple; for nonzero f, they are nonlinearly coupled and have to be solved iteratively. We note that dropping the rigid-lid approach would imply a contribution of ζ to the local water depth, leaving us with a set of three coupled hydrodynamic equations.

[24] Once the hydrodynamics is known, the components Q_m^n of the bed load sediment flux follow from (repeated) convolution sums in space and time. The components C_m^n of the suspended load concentration are obtained from a linear system. For the seabed evolution (equation (8)) we finally write $dH_m/d\tau = B_m$, where B_m is the mth component of the bed evolution due to both bed load and suspended load at time τ. We advance in the slow morphodynamic time using a semi-implicit scheme

$$H_m^{\mathrm{new}} = H_m + \frac{B_m}{\left(\frac{1}{\Delta\tau}\right) - \omega_m}, \tag{21}$$

with time step $\Delta\tau$ and where ω_m is the linear growth rate corresponding to the mth mode with wave number $k_m \equiv km$.

4. Results

4.1. Evolution Toward Equilibrium

[25] First, we investigate the evolution of the linearly most unstable mode in the nonlinear regime, in the case of a symmetric M_2 tidal forcing. To a periodic domain with wavelength $L = L_{\mathrm{fgm}}$ and flow angle $\vartheta = \vartheta_{\mathrm{fgm}}$, we introduce a slightly perturbed flat seabed according to equation (13), with $H_1/H = 0.01$. The finite amplitude evolution now consists of the following stages (Figure 4a): (1) exponential growth according to linear theory; (2) non-

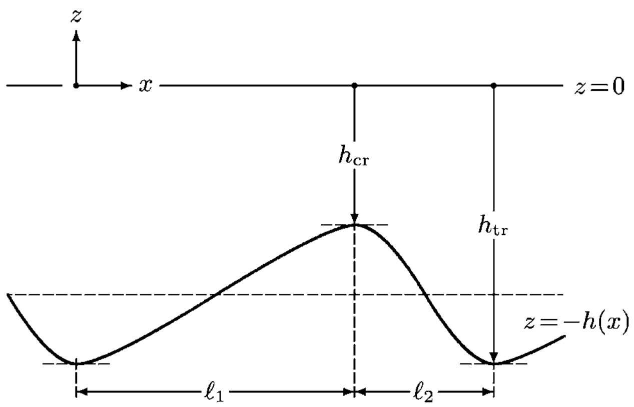

Figure 5. Definition of the quantities required in the definitions of relative bank height h_{rel} and profile asymmetry A in equations (23) and (24), respectively.

linear generation of higher harmonics that deform the sinusoidal shape; and (3) evolution toward an equilibrium profile, satisfying

$$\frac{\partial h}{\partial \tau} = 0, \qquad \text{for all } x. \tag{22}$$

This behavior appears to be universal, even though the details are sensitive to changes in the model parameters such as the basic flow representation, Coriolis force, wave activity, the type of transport, and transport parameters. Of particular interest is the equilibrium bank height, which we define as a fraction of the maximum water depth according to

$$h_{rel} = 1 - \frac{h_{cr}}{h_{tr}}. \tag{23}$$

Here h_{cr} and h_{tr} are the water depths above crest and trough, respectively (Figure 5). We conducted a set of numerical experiments for different values of the model parameters (Figure 6, Table 2). The simulations seem to indicate that for a given wavelength the equilibrium profile is unique. We make the following observations.

[26] 1. Bed load transport leads to highly nonlinear shapes with spiky crests and flat troughs, while suspended load transport leads to more sinusoidal shapes with lower, flattened crests (Figure 4a). This difference is also reflected in the corresponding Fourier spectra H_m (Figure 4c), which are real valued due to symmetry. The steepest slopes range between 1:1000 and 1:100 and are highest for bed load transport.

[27] 2. The Coriolis force is a destabilizing mechanism that leads to higher banks (Figure 6a) and shorter timescales. Its physical role is similar to that in the stage of formation, as explained in section 1. Coriolis effects continue to enhance the frictionally induced flow deflection around features with a counterclockwise orientation, thus amplifying bank growth. In equilibrium, this can only be balanced by stronger slope effects, which in turn requires a larger equilibrium bank height.

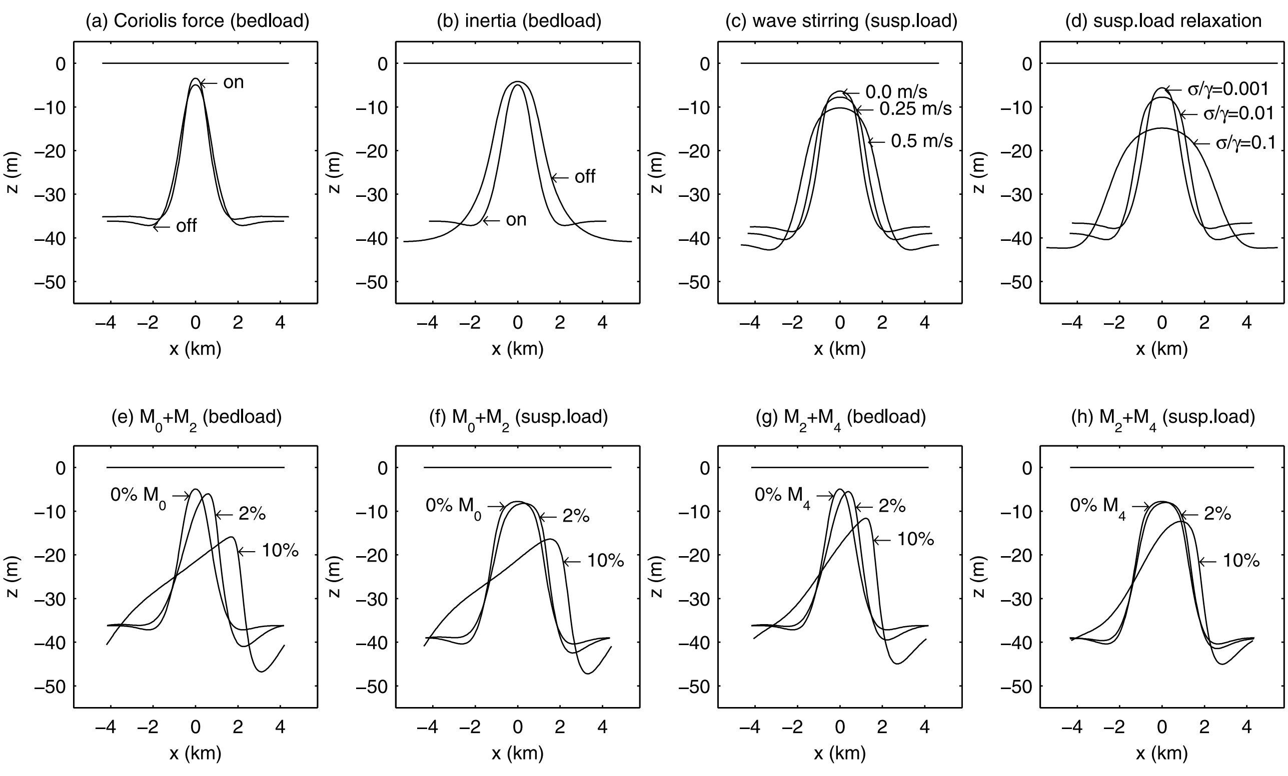

Figure 6. Properties of the equilibrium profiles for both bed load transport and suspended load transport (details of the simulations are shown in Table 2). Note that each profile has its own wavelength and orientation.

Table 2. Overview of Numerical Simulations, Each Case Being Defined Relative to One of the Two Default Cases 0_b and 0_s

No.[a]	Description	L,[b] km	ϑ,[b] deg	h_{cr}, m	h_{tr}, m	h_{rel}, %	A	c_{mig}, m yr^{-1}
0_b	**reference bed load**[c]	**8.4**	**28**	**5.0**	**37.2**	**87**		
0_s	**reference suspended load**[c]	**8.7**	**27**	**7.8**	**40.4**	**81**		
A_b	Coriolis force[d]	8.8	36	3.5	35.8	90		
A_s	Coriolis force[d]	9.1	35	5.8	38.8	85		
B_{b1}	$r \to r/2$	10.7	32	6.5	38.7	83		
B_{b2}	$r \to 2r$	6.5	27	5.1	37.4	87		
B_{s1}	$r \to r/2$	11.5	30	10.8	42.1	74		
B_{s2}	$r \to 2r$	6.7	26	7.3	39.7	82		
C_{b1}	$\lambda \to \lambda/2$	6.7	24	3.8	36.5	90		
C_{b2}	$\lambda \to 2\lambda$	10.9	33	7.0	38.3	82		
C_{s1}	$\lambda \to \lambda/2$	6.9	23	6.4	40.0	84		
C_{s2}	$\lambda \to 2\lambda$	11.5	32	9.9	40.6	76		
D_b	neglecting $\partial/\partial t$	10.8	23	4.2	40.9	90		
D_s	neglecting $\partial/\partial t$	11.4	22	5.1	41.9	88		
E_{b1}	U_w = 0.0 m s^{-1}	8.3	28			no equilibrium found		
E_{b2}	U_w = 0.5 m s^{-1}	8.5	28	7.1	39.7	82		
E_{s1}	U_w = 0.0 m s^{-1}	8.5	27	6.4	38.6	84		
E_{s2}	U_w = 0.5 m s^{-1}	9.3	28	10.2	42.8	76		
F_{s1}	$\sigma/\gamma = 10^{-3}$	8.5	29	5.6	37.9	85		
F_{s2}	$\sigma/\gamma = 10^{-1}$	10.9	22	14.9	42.4	65		
G_{b1}	2% M_0[e]	8.3	29	6.0	41.0	85	0.7	1.4
G_{b2}	10% M_0[e]	8.4	29	15.9	46.8	66	1.6	4.4
G_{s1}	2% M_0[e]	8.7	28	8.2	42.5	81	0.4	0.9
G_{s2}	10% M_0[e]	8.8	28	16.4	47.2	65	1.4	4.1
H_{b1}	2% M_4[f]	8.3	29	5.5	39.5	86	0.5	1.1
H_b2	10% M_4[f]	8.1	30	11.6	45.0	74	1.5	3.2
H_{s1}	2% M_4[f]	8.7	28	8.0	41.5	81	0.2	0.6
H_s2	10% M_4[f]	8.6	29	12.3	45.0	73	1.2	2.9

[a]Subscripts b and s refer to bed load and suspended load, respectively.
[b]From fastest growing mode from linear theory.
[c]Default parameter values from Table 1 (except $f = 0$, taken for computational convenience) Tide, $j_0 = 0$, $j_2 = 1$ m s^{-1}, $j_4 = 0$; bed load, $\mu_b = 1$, $\mu_s = 0$; suspended load, $\mu_b = 0$, $\mu_s = 1$; truncation parameters, $M = 16$, $N = 3$.
[d]Corresponding to a latitude of 52°N (Table 1).
[e]Sum of amplitudes kept constant: $j_0 + j_2 = 1$ m s^{-1}, $M = 20$.
[f]Sum of amplitudes kept constant: $j_2 + j_4 = 1$ m s^{-1}, $\varphi_4 = 0$, $M = 20$.

[28] 3. Increasing the bed friction coefficient or decreasing the bed slope coefficient shortens the preferred wavelength from linear theory, generally leading to higher equilibrium banks (Table 2).

[29] 4. Omitting the inertial terms $\partial u/\partial t$, $\partial v/\partial t$, and $\partial c/\partial t$ in equations (1), (2), and (6), respectively, results in significantly higher equilibrium banks (Figure 6b). This effect is strongest for suspended load as it involves omitting the inertia of the sediment concentration, as well.

[30] 5. Wind waves suppress bank height, and in the case of bed load transport under symmetrical flow conditions, their presence is required for convergence to an equilibrium. Increasing wave activity (larger values of U_w) leads to lower equilibrium banks (Figure 6c).

[31] 6. The degree of crest flattening appears to scale with the suspended load relaxation parameter σ/γ (Figure 6d). Like the linear case, in the limit $\sigma/\gamma \downarrow 0$, this relaxation effect is lost, and suspended load transport behaves as bed load transport.

[32] Note that any parameter change in the model affects both the characteristics of the fastest growing mode and its finite amplitude behavior. This explains the variations in wavelength (Figure 6) and orientation (see also Table 2).

[33] Which values of the spatial truncation number M are appropriate depends on the flow conditions and mode of transport. Taking $M = 16$ usually works, and for smoother profiles (suspended load, strong wind wave activity, neglecting the Coriolis force), even lower values suffice. For the temporal truncation number we take $N = 3$, which accounts for the higher harmonics. Higher values of N merely slow down the computation, without improving the morphodynamic results.

4.2. Tidal Asymmetry

[34] The finite amplitude morphodynamics is sensitive to the degree of asymmetry in the tidal forcing. Asymmetry is usually caused by the presence of a small M_0 component or an M_4 component, besides the dominant M_2 component of the tide. This asymmetry turns out to affect the resulting equilibrium profiles in three ways: they display (1) asymmetry, (2) migration, and (3) a reduction in height.

[35] In order to quantify the left-right asymmetry, we define

$$A = \log \frac{\ell_1}{\ell_2}. \tag{24}$$

Here ℓ_1 and ℓ_2 are the horizontal distances from crest to trough, measured on both sides of the profile (Figure 5). We chose a logarithmic scale such that a fully symmetric profile has $A = 0$, asymmetric ones lead to a nonzero A, and reversing an asymmetric profile (left-right) merely leads to a sign change. We find asymmetric shapes with A values of the order 1 (Figures 6e–6h, Table 2) for M_0 and M_4 amplitudes up to 10% of U. We further observe that an increase in tidal asymmetry leads to an increase in profile

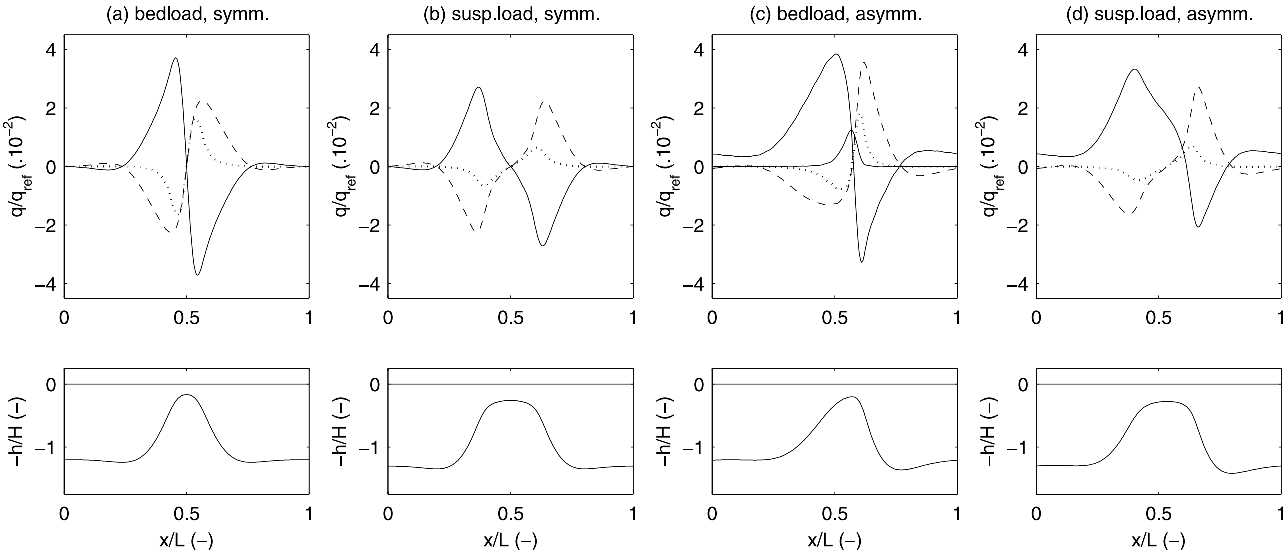

Figure 7. Different contributions to the tidally averaged sediment flux. Four cases are shown: (a) bed load subject to symmetric tide, (b) suspended load and symmetric tide, (c) bed load and asymmetric tide, (d) suspended load and asymmetric tide. Plotted are q^{drag} (solid lines), $q^{\text{sl,tide}}$ (dashed lines), and $q^{\text{sl,wave}}$ (dotted lines). Figure 7c contains two solid lines: one for the tidal contribution (highest curve) and one for the residual transport of wind wave-eroded material (lowest curve). The fluxes have been made dimensionless against the reference fluxes $q_{\text{ref}} = \alpha_{b,s}U^3$.

asymmetry, as well. Unscaled values of steepest bank slopes are about 1:100.

[36] A migrating equilibrium, for which equation (22) no longer holds, is characterized by

$$h = h\left(x - c_{\text{mig}}\tau\right), \tag{25}$$

with migration rate c_{mig}. Only in this shape-preserving case is the migration rate a well-defined quantity which can be estimated from the numerical simulations according to

$$c_{\text{mig}} = \frac{-B_m}{ikmH_m}, \tag{26}$$

where H_m and B_m are the Fourier components of the topography and the bed evolution, respectively. In a shape-preserving equilibrium of the form of equation (25), this quantity is real and identical for all m. The numerical experiments show that the migration rates of the nonlinear equilibrium are close to the ones obtained using linear theory (Table 2).

[37] More important, introducing asymmetry in the tidal forcing significantly reduces equilibrium height, especially when the M_0 component is responsible for the asymmetry (Figures 6e–6f, Table 2). The relatively steep lee slope requires larger values of the spatial truncation number M than in the symmetric case, with M = 20 usually being sufficient.

4.3. Physical Mechanisms

[38] We now focus on the physical mechanisms behind the equilibrium state. The physical mechanisms of bank formation in the linear stage have already been explained in section 3.1 and the references cited there. As we will explain below, it is convenient to distinguish the following physically different contributions to the tidally averaged sediment flux:

$$\begin{aligned} q_b^{\text{drag}} &= \alpha_b\left(\langle|\mathbf{u}|^2u\rangle + \frac{U_w^2 j_0}{2(h/H)^2 h}\right), & q_s^{\text{drag}} &= \langle cu\rangle, \\ q_{b,s}^{\text{sl,tide}} &= \alpha_{b,s}\lambda\langle|\mathbf{u}|^2\rangle\frac{\partial h}{\partial x}, & q_{b,s}^{\text{sl,wave}} &= \frac{\alpha_{b,s}\lambda U_w^2}{2(h/H)^2}\frac{\partial h}{\partial x}. \end{aligned} \tag{27}$$

The so-called bed load drag contribution consists of two terms: a tidally induced component and one related to the transport by residual currents of wind wave-eroded material. In the absence of an M_0 component, j_0 = 0, and the latter component vanishes. In the suspended load case, both components are contained in the flux $\langle cu\rangle$. The slope contributions, related to tidal flow and wind wave stirring, are of similar form for both modes of sediment transport.

[39] First, we consider a symmetric forcing and bed load transport only. In equilibrium the tidally averaged bed load sediment flux across the bank is constant; by symmetry, it must be zero. This implies the following balance:

$$q_b^{\text{drag}} + q_b^{\text{sl,tide}} + q_b^{\text{sl,wave}} = 0. \tag{28}$$

From Figure 7 we see that the drag contribution is destabilizing as it carries sediment from trough to crest. This is analogous to the linear stage of formation. In equilibrium, it is compensated by the joint effect of the gravitationally induced fluxes due to tidal flow and wave stirring. The former acts along the flanks, the latter mainly in the shallow area close to the crests. Reducing wave activity (smaller U_w) decreases the stabilizing effect, which leads to higher banks.

[40] For suspended load transport a similar equilibrium holds, in which the drag effects are replaced with the

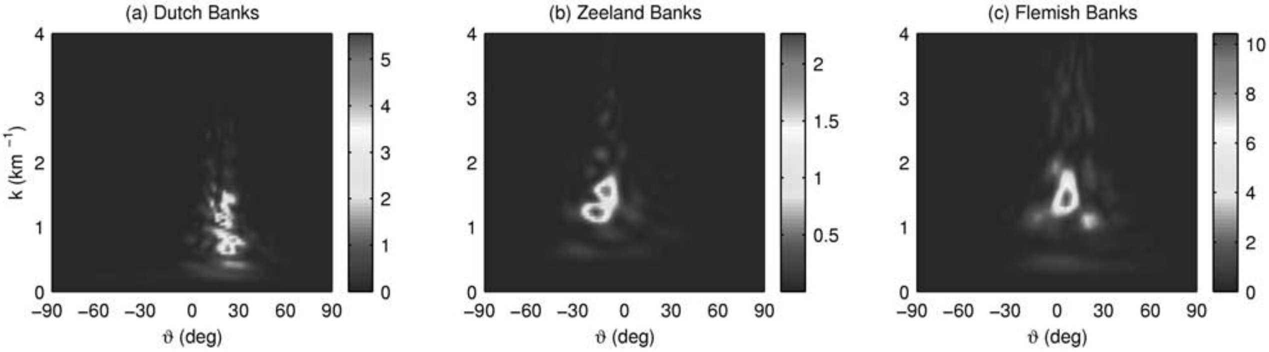

Figure 8. Fourier spectra of the seabed topography for the three boxed areas in Figure 1: (a) Dutch Banks, (b) Zeeland Banks, and (c) Flemish Banks. The angle ϑ has the principal flow direction, and k is the dimensional wave number. The plotted signal is proportional to the amplitude of the bed elevation. See color version of this figure at back of this issue.

difference between entrainment and deposition. Combining equations (6) and (8), we find, after taking the tidal average, that

$$q_s^{\text{drag}} + q_s^{\text{sl,tide}} + q_s^{\text{sl,wave}} = 0. \tag{29}$$

The temporal and spatial relaxation of suspended load causes the quantity q_s^{drag} to be smaller than the bed load drag term q_b^{drag}, assuming $\alpha_b = \alpha_s$. Figure 7 shows that this has a smoothing effect on the equilibrium topography.

[41] Asymmetry disrupts the picture sketched here, causing a net sediment flux in the direction of the tidal asymmetry. In a migrating equilibrium of the form of equation (25) the sum of the separate contributions is no longer zero, as in equations (28) and (29). Instead, it should equal the sediment flux required to maintain shape-preserving propagation at celerity c_{mig}. From equation (25), it follows that $\partial h/\partial\tau = -c_{\text{mig}}\, \partial h/\partial x$, which in turn leads to

$$q_{b,s}^{\text{drag}} + q_{b,s}^{\text{sl,tide}} + q_{b,s}^{\text{sl,wave}} = -c_{\text{mig}} h + \text{const.} \tag{30}$$

From Figure 7, it is seen that the drag contribution in the direction of the asymmetry (from left to right along the stoss side) is enhanced. This also applies to the slope contributions along the lee side. As already noted in section 4.2, asymmetric equilibrium profiles are lower than symmetric ones. Therefore wind wave stirring under asymmetric conditions turns out to have a smaller effect than in the symmetric case.

[42] Finally, we note that equations (28), (29), and (30) express tidally averaged balances. Hence the instantaneous effects need not be in balance; they may even differ in order of magnitude. This emphasizes the dynamic nature of the equilibrium, which allows small intratidal bed changes as long as they compensate each other throughout the tidal cycle.

5. Comparison With North Sea Data

5.1. Observations

[43] In this section we compare the results from the nonlinear theory with data from the North Sea. The nonlinear analysis provides new characteristics of tidal sandbanks in morphodynamic equilibrium: (relative) bank height, asymmetry, and migration as well as other more qualitative characteristics such as shape. Wavelength and orientation were already predicted by the linear theory. Because there is no evidence of significant topographic changes over the last century, we may assume that the banks in the North Sea are indeed in or close to a morphodynamic equilibrium state. Observations suggest that this equilibrium is maintained by present-day flow conditions (see *Trentesaux et al.* [1999] for the Middelkerke Bank, one of the Flemish Banks).

[44] We explored the available data (Figure 1a) in two ways: by (1) identifying and analyzing the crest and trough positions and by (2) transforming into Fourier space. Figure 1b reveals that large-scale wavy patterns are present almost everywhere in the domain, with varying bed amplitude. Three sites with more pronounced banks catch the eye (Figure 1): the Dutch Banks (upper box), the Zeeland Banks (center box), and the Flemish Banks (lower box). It should be noted that it is unclear whether the latter two should be classified as open-shelf ridges (tidal sandbanks) or shoreface-connected ridges (more details on this classification can be found in the work of *Dyer and Huntley* [1999]).

[45] For each of these areas the Fourier spectrum shows prevailing wavelength and orientation (Figure 8 and Table 3). The orientation has been taken relative to the principal tidal flow direction, which has been extracted from the numerical work by *Van der Molen and De Swart* [2001]. We use numerical results because we did not find data that also provide estimates of the components in the basic flow equation (11), which we need as input for our model application (section 5.2). The dominant observed wavelength is of the order of 6–10 km (Dutch Banks) and 5 km (Zeeland Banks and Flemish Banks). The Dutch Banks and the Flemish Banks have a dominant orientation counterclockwise to this flow angle, of ~25° and ~6°, respectively. In contrast, the Zeeland Banks have a clockwise orientation. This supports the idea that they are shoreface-connected ridges rather than tidal sandbanks, and we will exclude them from further analysis.

[46] To obtain a more detailed impression of these banks, we extracted a typical bank profile from each of the two remaining locations (Figure 9, Table 3). Each of

Table 3. Typical Banks at Two Sites in the Southern Bight of the North Sea: Observations Versus Model Application

	Dutch Banks	Flemish Banks
	Location	
Northing, easting, km	5826, 540	5710, 464
Latitude	52°N40′	51°N30′
	Observations	
Wavelength L,[a] km	5.7–9.8	4.5
Orientation ϑ,[a,b] deg	25	6
Bank height h_{rel},[c] %	26	61
Asymmetry A[c]	1.3	0.2
	Conditions (Model Input)	
Average water depth H, m	28.9	28.7
Flow angle,[d,e] deg	66.7	59.0
U,[e] m s^{-1}	0.75	0.80
j_0,[e] m s^{-1}	0.01	0.00
j_2,[e] m s^{-1}	0.69	0.74
j_4,[e] m s^{-1}	0.08	0.08
φ_4,[e] deg	36.4	127.5
	Model Output	
L_{fgm}, km		
Bed load	7.2	7.5
Suspended load	7.6	7.7
ϑ_{fgm}, deg		
Bed load	39	38
Suspended load	38	37
h_{rel}, %		
Bed load	78	84
Suspended load	76	80
A		
Bed load	1.6	−1.5
Suspended load	1.2	−0.5
c_{mig}, m yr^{-1}		
Bed load	1.9	−1.6
Suspended load	1.8	−1.3

[a]From Fourier spectrum (Figure 8).
[b]Relative to the principal flow direction (based on *Van der Molen and De Swart* [2001]).
[c]From profiles (Figure 9).
[d]In degrees counterclockwise to west-east direction.
[e]Based on *Van der Molen and De Swart* [2001].

these profiles is taken as the average over an along-bank stretch of several hundreds of meters.

5.2. Model Input

[47] The next step is to calculate the equilibrium banks which would exist at the two remaining locations (Dutch Banks and Flemish Banks), according to the morphodynamic model we developed. The hydrodynamic conditions, needed as model input, have been taken from the numerical work of *Van der Molen and De Swart* [2001]. Their simulations cover the southern North Sea, and the resolution of 10 km is such that the presence of sandbanks must be neglected. This is favorable as the required model input indeed corresponds to flat-bed conditions. The two locations turn out to have an elliptical tide, albeit of small eccentricity. To obtain the required input form, given by equations (10) and (11), we projected the tidal signal onto the principal tidal axis (tidal components given in Table 3). The Coriolis parameter is adjusted to local latitude, whereas the other parameter values have been taken from Table 1. Numerical truncation parameters have been set at $M = 20$ and $N = 3$.

5.3. Comparison

[48] Now, we compare the model results with the observations. We stress that the model has not been tuned in any way to obtain better agreement.

[49] For the chosen parameters, linear theory predicts wavelengths of ~7 km. This roughly agrees with the wavelength of the observed profiles. The wavelength of the fastest growing mode appears to be insensitive to differences in the hydrodynamic conditions. In addition, it turns out that the angle between flow and bank crest is overestimated by linear theory, by as much as 15°–30°.

[50] Bank height, as estimated by nonlinear theory, appears to overestimate the observations, especially at the Dutch Banks. The spikiness in the bank crests is found in both model results and observations. This also holds for the

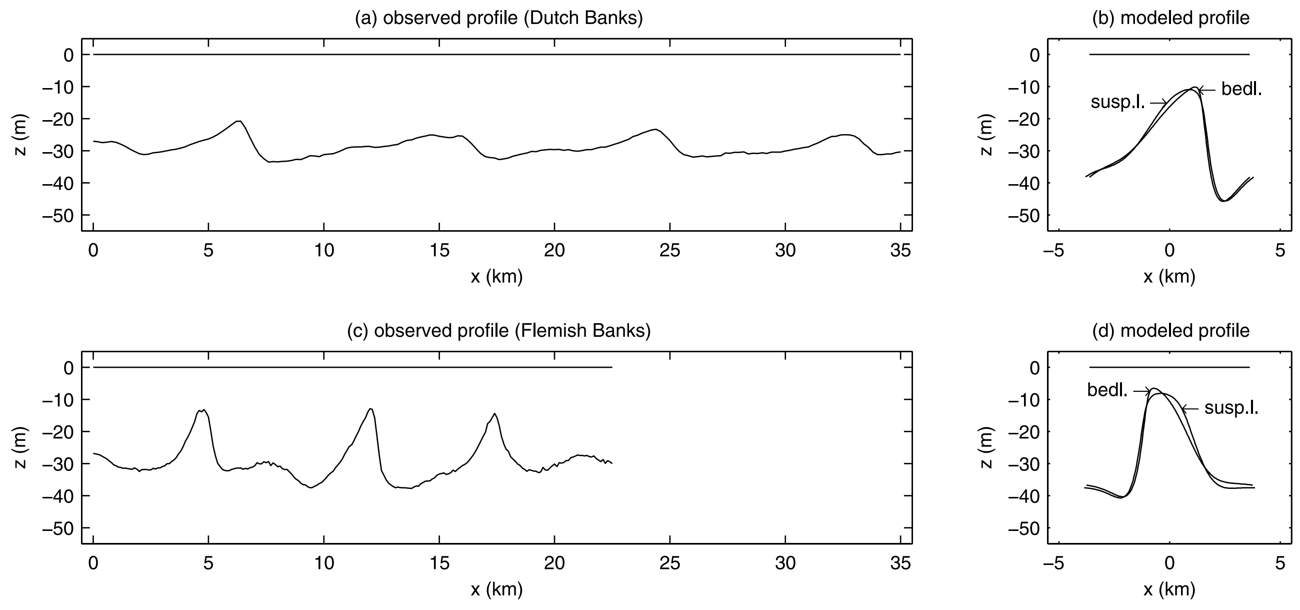

Figure 9. Tidal sandbanks at two locations in the North Sea. (a) Observed profile at Dutch Banks. (b) Modeled profile for both bed load and suspended load transport at Dutch Banks. (c) Observed profile at Flemish Banks. (d) Modeled profile for both bed load and suspended load transport at Flemish Banks.

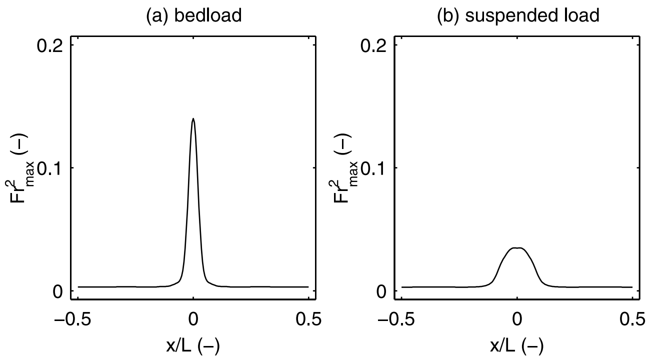

Figure 10. Maximum values of the Froude number throughout the tidal cycle for (a) bed load and (b) suspended load (cases $A_{b,s}$ in Table 2).

notion that asymmetric banks are generally lower than the symmetric ones. For the Dutch Banks we find qualitative agreement between the asymmetries in bank shape and tidal forcing. The tidal asymmetry at the Flemish Banks is small and leads to a modeled profile with small asymmetry, yet pointing in the wrong direction. Finally, we notice again from the model results that the temporal and spatial relaxation of suspended sediment has a smoothing effect on the dynamics, resulting in lower values of bank height, asymmetry, and migration.

[51] Migration rates predicted by the model are of the order of a meter per year. The data, a snapshot of the present bathymetry, neither confirm nor contradict this result. However, we should note that in reality, there is little evidence of sandbank migration. Furthermore, the uncertainty in the sediment transport coefficient $\alpha_{b,s}$ also causes uncertainty in our migration estimates.

6. Discussion

6.1. Physics

[52] The rigid-lid assumption, which simplifies the solution procedure, is justified if the Froude number remains small also in the finite amplitude regime. The maximum (squared) Froude number, maximized over the tidal cycle, is defined by

$$Fr^2_{\max} \equiv \max_t\left(\frac{u^2+v^2}{gh}\right). \tag{31}$$

It is highest at the crests of banks in equilibrium (Figure 10). For the spiky equilibrium shapes typical of bed load transport we find maximum values of $\sim$0.1. For the lower profiles of suspended load, this is nearly an order of magnitude smaller. We conclude that the rigid-lid assumption is justified, although for the bed load case, it may be worthwhile to investigate the consequences of dropping the rigid-lid assumption. However, this is not a straightforward extension of the present approach. The existence of a spatially uniform basic state heavily relies on the rigid-lid assumption. Computationally, the dimension of the hydrodynamic problem increases considerably now that ζ can no longer be eliminated.

[53] The results show that the linear theory behaves well up to amplitudes of $\sim 0.2H$ (Figure 4), beyond which nonlinear effects dominate. The migration rates from the linear stage and the finite amplitude equilibrium turn out to be nearly the same. Underlying this equilibrium is a balance between destabilizing fluxes due to the drag of tidal flow and stabilizing fluxes due to downslope transport. The latter consists of both tidally induced downslope transport and wind wave-eroded material. For the typical case of bed load transport subject to a symmetrical tide, such a stirring mechanism is even required to obtain equilibrium. In other cases, wave stirring turns out to lower and smooth the equilibrium profiles.

[54] Comparison with observations from the North Sea shows that the model generally tends to overpredict bank height. This can be due to the lack of a physical mechanism (rise and fall of free surface during tidal cycle). We further noticed a discrepancy between the angle of the fastest growing mode from linear theory and those of observed banks. *Huthnance* [1982a] already noted that the orientation especially is sensitive to the uncertain formulation of sediment transport and is probably also susceptible to, for example, the trend of an adjacent coastline. Alternatively, differences between the direction of depth-averaged flow and the bed shear stress could partly account for this deficiency.

[55] Our approach does not incorporate the dynamics of sand waves, which require a description of the vertical flow structure at shorter length scales of hundreds of meters [*Hulscher*, 1996]. Hence we are unable to investigate finite amplitude sandbank dynamics as a result of nonlinear sand wave interaction. Such a mechanism has been proposed by *Komarova and Newell* [2000], and we consider it worthwhile to investigate it further in a three-dimensional setting, allowing to test it from a more observational perspective.

[56] The uncertainty in sediment transport coefficients α_b and α_s is reflected in the timescales of morphodynamic evolution, which is of the order of centuries. Some parameters, assumed constant in the model, may actually vary on this timescale, such as mean water depth owing to sea level rise. Even though present-day sea level rise is relatively strong, it has been significantly smaller over the past couple of millennia [*Douglas*, 1995]. Hence it does not significantly harm the present results, but we consider it an important mechanism when aiming at long-term morphodynamic predictions for the future.

[57] The model we have developed is idealized as our main focus is on the physics from a qualitative point of view. For example, we have studied the two transport modes in an isolated way, i.e., either bed load or suspended load transport. In reality, these modes occur simultaneously, with their relative importance depending on grain size. However, modeling this grain size dependence properly would also require the inclusion of a critical flow velocity (or critical shear stress) for sediment motion. Part of this grain size dependence stems from this threshold [*Idier*, 2003]. We considered this beyond the scope of the present study. Finally, it is also worthwhile to investigate the influence of grain size variations on sandbank dynamics, taking into account hiding and exposure (as studied by *Walgreen et al.* [2003] for shoreface-connected ridges).

6.2. Surviving Mode

[58] A restrictive property of the model is its spatial periodicity. We fixed the value to the preferred wavelength

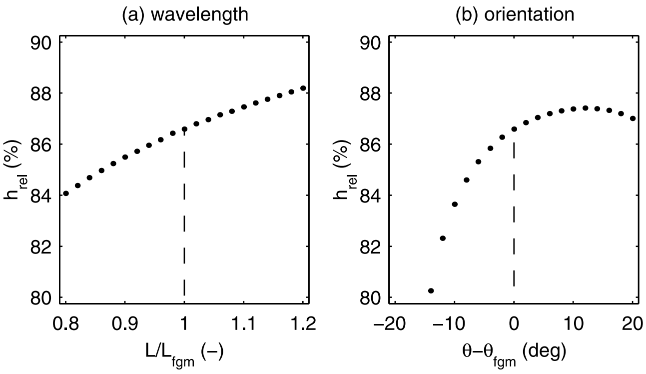

Figure 11. Dependence of equilibrium bank height h_{rel} on (a) imposed wavelength and (b) flow orientation, both relative to the fastest growing mode (case A_b in Table 2).

obtained from linear theory, thus imposing the wavelength of growing sandbanks. Although this is a common approach followed in other fields of morphodynamic modeling (for example, in the study of shoreface-connected ridges by *Calvete et al.* [2002]), the finite amplitude wavelength selection within the system cannot be studied. In their weakly nonlinear study of alternate bar evolution in rivers, *Schielen et al.* [1993] allowed for small changes in wavelength. Figure 11a shows the sensitivity of equilibrium bank height on the imposed wavelength, in a region around $L = L_{\mathrm{fgm}}$. It shows that for a longer wavelength the system tends to higher equilibrium banks. This topic needs further investigation.

6.3. Two-Dimensional Topographies

[59] In this paper we restrict ourselves to topographies that vary in one horizontal dimension only. This choice is supported by the predominantly one-dimensional horizontal character of real sandbanks. It also simplifies the analysis but forces us to externally impose the angle ϑ between the basic flow and the direction of topographic variations. Choosing the preferred angle from linear theory is the most logical choice. However, nonlinear effects may alter the preferred bank orientation. For example, Figure 11b shows that the angle ϑ_{fgm}, for which initial growth is largest, may not lead to the highest equilibrium banks. In a two-dimensional approach the preferred angle emerges naturally within the system. We therefore no longer need to impose it externally; it may even adjust itself while the banks are growing.

7. Conclusions

[60] The nonlinear morphodynamic model presented in this paper is capable of producing evolution toward non-trivial equilibrium states, which we associate with equilibrium profiles of tidal sandbanks. Equilibrium heights, varying between 60 and 90% of the maximum water depth, and their shapes depend on the type of transport and the hydrodynamic conditions. In particular, bed load leads to spiky equilibrium banks with flat troughs, whereas the relaxation of suspended load leads to lower and more rounded crests. The underlying (tidally averaged) balance is between the destabilizing sediment flux due to fluid drag and the downslope transport induced by both tidal flow and wind wave stirring. Tidal asymmetry produces asymmetric equilibrium profiles, which migrate at a rate of the order of that predicted from linear theory. This asymmetry, wind waves, and, furthermore, the inertia of the tide have a damping effect on equilibrium heights.

[61] We claim that fully resolving the dynamics on both the fast and slow timescales is essential to capture the physics that determine the cross-sectional shape of tidal sandbanks. The assumptions made in earlier studies to simplify the dynamics on the fast tidal timescale affect the results significantly. In particular, using a block flow and omitting inertial terms [*Huthnance*, 1982a, 1982b; *Roos et al.*, 2002; *Idier and Astruc*, 2003] is too crude a means of mimicking the nonlinear morphodynamics caused by an M_2 tide.

[62] Comparison with information on large-scale features extracted from North Sea bathymetric data gives fair agreement between observed and modeled bank heights and shapes, albeit mainly qualitatively. The comparison is complicated by the small number of banks, the uncertainty in the input, and along-bank variations in the observed profiles.

[63] **Acknowledgments.** We thank Sandra Passchier and Ad van der Spek from TNO-NITG/Hydrographic Service (Utrecht, Netherlands) for providing the bathymetric data of the Dutch continental shelf. We are also grateful to the department Waterwegen Kust of the Administratie Waterwegen en Zeewezen (Oostende, Belgium) for granting us permission to use their measurements of the Flemish Banks and to Vera van Lancker and Samuel Deleu of Ghent University for providing the data set. Johan van der Molen is thanked for supplying the hydrodynamic conditions from his numerical model results. We are grateful to Huib de Swart and a second, anonymous reviewer for their comments. This research was carried out within the EU-project HUMOR, contract EVK3-CT-2000-00037.

References

Calvete, D., H. E. De Swart, and A. Falqués (2002), Effect of depth-dependent wave stirring on the final amplitude of shoreface-connected sand ridges, *Cont. Shelf Res.*, *22*, 2763–2776.

De Vriend, H. J. (1990), Morphological processes in shallow tidal seas, in *Residual Currents and Long Term Transport*, *Coastal Estuarine Stud.*, vol. 38, edited by R. T. Cheng, pp. 276–301, Springer-Verlag, New York.

Douglas, B. C. (1995), Global sea level change: Determination and interpretation, *Rev. Geophys.*, *33*, 1425–1432.

Dyer, K. R., and D. A. Huntley (1999), The origin, classification and modelling of sand banks and ridges, *Cont. Shelf Res.*, *19*, 1285–1330.

Hulscher, S. J. M. H. (1996), Tidal-induced large-scale regular bed form patterns in a three-dimensional shallow water model, *J. Geophys. Res.*, *101*, 20,727–20,744.

Hulscher, S. J. M. H., H. E. De Swart, and H. J. De Vriend (1993), The generation of offshore tidal sand banks and sand waves, *Cont. Shelf Res.*, *13*, 1183–1204.

Huntley, D. A., J. M. Huthnance, M. B. Collins, C.-L. Liu, R. J. Nicholls, and C. Hewitson (1993), Hydrodynamics and sediment dynamics of North Sea sand waves and sand banks, *Philos. Trans. R. Soc. London, Ser. A*, *343*, 461–474.

Huthnance, J. M. (1982a), On one mechanism forming linear sand banks, *Estuarine Coastal Shelf Sci.*, *14*, 74–99.

Huthnance, J. M. (1982b), On the formation of sand banks of finite extent, *Estuarine Coastal Shelf Sci.*, *15*, 277–299.

Idier, D. (2003), Note on grain size dependency in morphodynamic modelling, or the importance of the critical shear stress, *CE & M Res. Rep. 2003W-004/WEM-002*, Univ. of Twente, Enschede, Netherlands.

Idier, D., and D. Astruc (2003), Analytical and numerical modeling of sandbanks dynamics, *J. Geophys. Res.*, *108*(C3), 3060, doi:10.1029/2001JC001205.

Kenyon, N. H., R. H. Belderson, A. H. Stride, and M. A. Johnson (1981), Offshore tidal sand banks as indicators of net sand transports and as potential deposits, in *Holocene Marine Sedimentation in the North Sea Basin*, edited by S. D. Nio, R. T. E. Schuttenhelm, and T. C. E. Weering, pp. 257–268, Blackwell Sci., Malden, Mass.

Komarova, N. L., and A. C. Newell (2000), Nonlinear dynamics of sand banks and sand waves, *J. Fluid Mech.*, *415*, 282–312.

Parker, G. (1978), Self-formed straight rivers with equilibrium banks and mobile bed. part 1. The sand-tilt river, *J. Fluid Mech.*, *89*, 109–125.

Pattiaratchi, C., and M. Collins (1987), Mechanisms for linear sandbank formation and maintenance in relation to dynamical oceanographic observations, *Prog. Oceanogr.*, *19*, 117–176.

Robinson, I. S. (1983), Tidally induced residual flows, in *Physical Oceanography of Coastal and Shelf Seas*, edited by B. Johns, pp. 321–356, Elsevier Sci., New York.

Roos, P. C., and S. J. M. H. Hulscher (2003), Large-scale seabed dynamics in offshore morphology: Modeling human intervention, *Rev. Geophys.*, *41*(2), 1010, doi:10.1029/2002RG000120.

Roos, P. C., S. J. M. H. Hulscher, B. G. T. M. Peters. and A. A. Németh (2001), A simple morphodynamic model for sand banks and large-scale sand pits subject to asymmetrical tides, paper presented at the RCEM Symposium 2001, Int. Assoc. for Hydraul. Res., Hokkaido, Japan.

Roos, P. C., S. J. M. H. Hulscher, and R. M. J. Van Damme (2002), Finite amplitude tidal sandbanks: Modelling one-dimensional equilibrium profiles, paper presented at the 28th International Conference on Coastal Engineering, Cardiff, U. K.

Schielen, R., A. Doelman, and H. E. De Swart (1993), On the nonlinear dynamics of free bars in straight channels, *J. Fluid Mech.*, *252*, 325–356.

Schuttelaars, H. M. (1998), Nonlinear long term equilibrium profiles in a short tidal embayment, in *Physics of Coastal Seas and Estuaries*, edited by J. Dronkers and M. B. A. M. Scheffers, pp. 337–343, A. A. Balkema, Brookfield, Vt.

Schuttelaars, H. M., and H. E. De Swart (1996), An idealized long-term morphodynamic model of a tidal embayment, *Eur. J. Mech. B*, *15*(1), 55–80.

Sekine, M., and G. Parker (1992), Bed-load transport on transverse slope, *J. Hydraul. Eng.*, *118*(4), 513–535.

Talmon, A. M., M. C. L. M. Van Mierlo, and N. Struiksma (1995), Laboratory measurements of the direction of sediment transport on transverse alluvial slopes, *J. Hydraul. Res.*, *33*, 495–517.

Trentesaux, A., A. Stolk, and S. Berné (1999), Sedimentology and stratigraphy of a tidal sand bank in the southern North Sea, *Mar. Geol.*, *159*, 253–272.

Van der Molen, J., and H. E. De Swart (2001), Holocene tidal conditions and tide-induced sand transport in the southern North Sea, *J. Geophys. Res.*, *106*, 9339–9362.

Van Rijn, L. C. (1993), *Principles of Sediment Transport in Rivers, Estuaries and Coastal Sea*, Acqua Publ., Amsterdam.

Vincent, C. E., A. Stolk, and C. F. C. Porter (1998), Sand suspension and transport on the Middelkerke Bank (southern North Sea) by storms and tidal currents, *Mar. Geol.*, *150*, 113–129.

Walgreen, M., H. E. de Swart, and D. Calvete (2003), Effect of grain size sorting on the formation of shoreface-connected sand ridges, *J. Geophys. Res.*, *108*(C3), 3063, doi:10.1029/2002JC001435.

Zimmerman, J. T. F. (1981), Dynamics, diffusion and geomorphological significance of tidal residual eddies, *Nature*, *290*, 549–555.

Zimmerman, J. T. F. (1982), On the Lorentz linearization of a quadratically damped forced oscillator, *Phys. Lett. A*, *89*, 123–124.

S. J. M. H. Hulscher, M. A. F. Knaapen, and P. C. Roos, Water Engineering and Management, Faculty of Engineering Technology, University of Twente, P.O. Box 217, 7500 AE Enschede, Netherlands. (s.j.m.h.hulscher@utwente.nl; m.a.f.knaapen@utwente.nl; p.c.roos@utwente.nl)

R. M. J. Van Damme, Department of Applied Mathematics, Faculty of Electrical Engineering, Mathematics and Computer Science, University of Twente, P.O. Box 217, 7500 AE Enschede, Netherlands. (r.m.j.vandamme@utwente.nl)

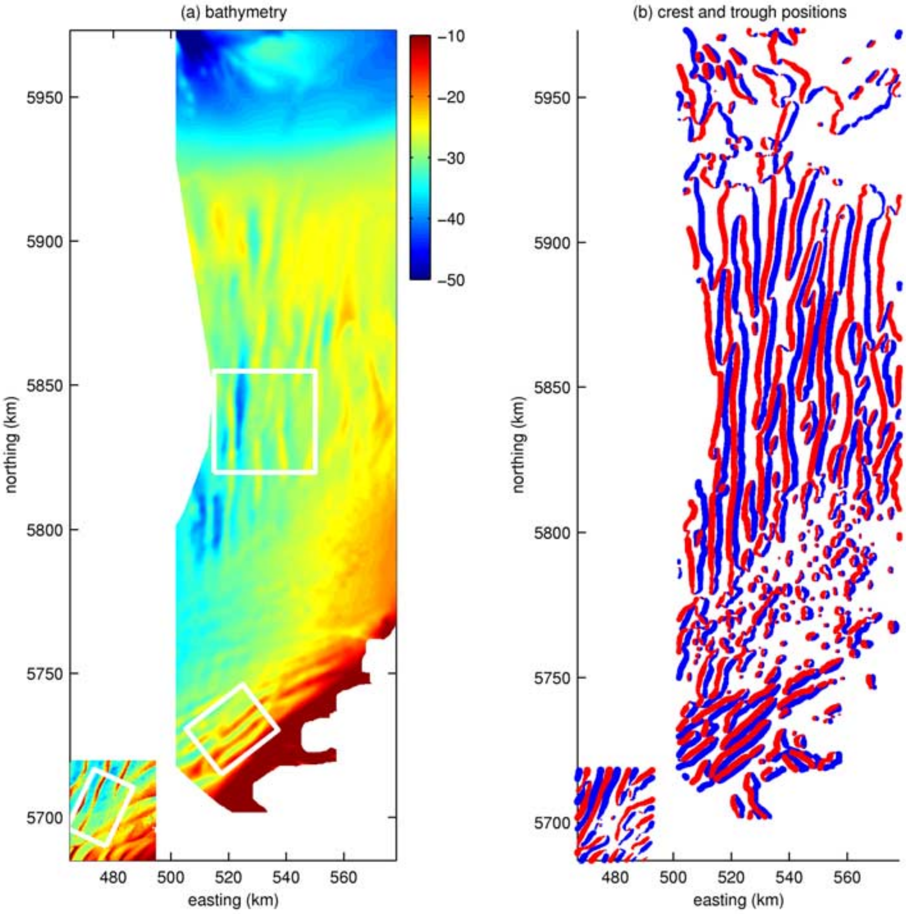

Figure 1. Seabed topography in the Southern Bight of the North Sea. (a) Bathymetry, showing three boxed areas to be analyzed further in section 5. Regions without data are indicated in white, such as the U.K. continental shelf (left) and the Dutch and Belgian mainland (bottom right). (b) Crest and trough positions of large-scale features (in red and blue, respectively), with line thickness proportional to bank height. See the acknowledgments for data sources.

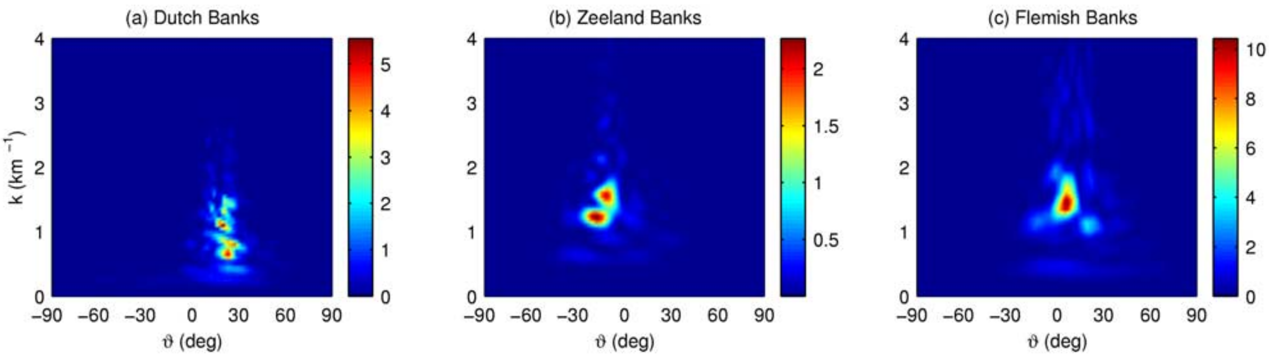

Figure 8. Fourier spectra of the seabed topography for the three boxed areas in Figure 1: (a) Dutch Banks, (b) Zeeland Banks, and (c) Flemish Banks. The angle ϑ has the principal flow direction, and k is the dimensional wave number. The plotted signal is proportional to the amplitude of the bed elevation.